Journal of the Meteorological Society of Japan

EARLY ONLINE RELEASE

The DOI for this manuscript is
DOI:10.2151/jmsj.2023-006
J-STAGE Advance published date: November 15th, 2022

Development of synoptic-scale disturbances over the tropical western North Pacific associated with the boreal summer intraseasonal oscillation and the interannual Pacific-Japan pattern

Ayako SEIKI[1], Yu KOSAKA[2], and Satoru YOKOI[1]

1. Dynamic Coupling of Ocean-Atmosphere-Land Research Program, Research Institute for Global Change, Japan Agency for Marine-Earth Science and Technology, Yokosuka, Japan

2. Research Center for Advanced Science and Technology, The University of Tokyo, Tokyo, Japan

Submitted in Feb., 2022

Revised in Aug., 2022

----

1) Corresponding author: Ayako Seiki Japan Agency for Marine-Earth Science and Technology, 2-15, Natsushima-cho, Yokosuka, Kanagawa 237-0061 JAPAN.

Email: aseiki@jamstec.go.jp

Tel: +81-46-867-9825

Fax: +81-46-867-9255

Abstract

The development mechanism of synoptic-scale disturbances over the tropical western North Pacific (WNP) associated with the boreal summer intraseasonal oscillation (BSISO) under different phases of the interannual Pacific-Japan (PJ) pattern is investigated. Intraseasonal convection is enhanced widely over the WNP for BSISO phases 5–7 in the positive PJ years, when seasonal-mean convective activity over the tropical WNP is enhanced. By contrast, developed convection is confined over the South China Sea in the negative PJ years. Similar features are also found in the horizontal distributions of eddy kinetic energy (*K'*) representing the activity of synoptic-scale disturbances and of tropical cyclone occurrences. The differences in location of intraseasonal convection and the activity of synoptic-scale disturbances between the positive and negative PJ years likely lead to different teleconnection to midlatitude East Asia. The non-PJ years show mixed features of the positive and negative PJ years. A *K'* budget analysis reveals that the energy conversion from eddy available potential energy to *K'* (PeKe) associated with synoptic convection primarily contributes to *K'* generation during the convectively active phases of the BSISO. The barotropic energy conversion from mean kinetic energy to *K'*, KmKe, is the second largest contributor to the *K'* increase in the lower troposphere, especially during the early stage of development of synoptic disturbances. Large *K'* produced by PeKe and KmKe in the tropics is advected to the subtropics by the mean flow in the late to mature stages of development. There are two factors that can determine

the different locations where synoptic disturbances develop associated with PeKe and KmKe. One is intraseasonal sea surface warming during convectively suppressed phases of the BSISO preceding the active phases. The other is convergence or shear of seasonal-mean horizontal winds associated with interannual fluctuations of monsoon westerlies over the WNP.

Keywords boreal summer intraseasonal oscillation; tropical synoptic disturbances; Pacific-Japan pattern

1. Introduction

The dominant intraseasonal oscillation (ISO) in the tropics during boreal summer is called the boreal summer intraseasonal oscillation (BSISO; Wang and Rui 1990; Lawrence and Webster 2002; Kikuchi et al. 2012; Kikuchi 2021). The BSISO is accompanied by deep convection and atmospheric circulation propagating northeastward and/or eastward over the warm pool in the tropics from the Indian Ocean to the western Pacific, while the Madden-Julian Oscillation (e.g., Madden and Julian 1971, 1972), the dominant intraseasonal mode in boreal winter, migrates only eastward along the equator. Numerous studies have been performed to clarify the mechanism of ISO propagation, and moisture buildup is known to play a fundamental role in the organization of ISO convection (e.g., Hendon and Salby 1994; Kemball-Cook and Weare 2001; Maloney and Hartmann 1998; Maloney 2009; Katsumata et al. 2013). While the ISO is an atmospheric phenomenon, it migrates with intraseasonal sea surface temperature (SST) fluctuations (e.g., Hendon and Glick 1997; Shinoda and Hendon 1998). These studies showed that the SST warms by anomalous insolation during the ISO convectively suppressed phase preceding the convection center of ISO and cools by reduced insolation and enhanced latent heat flux by strong winds during the active phases. This SST warming in the suppressed phase is one of the factors leading to moisture buildup through shallow convection and the organization of ISO convection (e.g., Johnson et al. 1999; Kikuchi and Takayabu 2004). Note that the convectively active period of BSISO in the tropical western North Pacific (WNP) corresponds to phases 5–8 in this study (see

Fig. 1 for general distributions of intraseasonal convection).

The ISO in the tropics has a hierarchical structure consisting of eastward-propagating cloud clusters and westward-propagating synoptic disturbances, while the ISO has been known as a planetary scale phenomenon (e.g., Nakazawa 1988). Meanwhile, the activity of synoptic-scale disturbances such as tropical cyclones (TCs) is modulated by the ISO through changes in the environmental field (e.g., Lau and Lau 1992; Liebmann et al. 1994; Maloney and Hartmann 2000; Camargo et al. 2009; Yoshida et al. 2014). These studies have shown that synoptic disturbances are activated in the convectively active and low-level westerly phases of the ISO. Especially regarding the BSISO, the TC activity is highest during BSISO phase 7 (e.g., Yoshida et al. 2014). Thus, synoptic disturbances constitute the ISO as internal disturbances and are affected by environmental changes induced by the ISO, resulting in an interacting relationship (e.g., Zhou and Li 2010).

These convectively-coupled ISOs in the tropics have been known to influence not only tropical but also extratropical circulation anomalies (e.g., Knutson and Weickmann 1987; Matthews et al. 2004). Seiki et al. (2021b; hereafter SKY21) investigated the relationship between the BSISO and intraseasonal fluctuations of the summertime tropical-extratropical teleconnection over the WNP called the Pacific-Japan (PJ) pattern, which is excited by anomalous convective activities over the tropical WNP (e.g., Nitta 1987; Kurihara and Tsuyuki 1987; Wakabayashi and Kawamura 2004; Kosaka and Nakamura 2006, 2010). The PJ pattern has been recognized as a meridional dipole of lower tropospheric circulation anomalies in interannual variability of seasonal mean fields, but it appears like a wave train pattern on shorter time scales such as intraseasonal and synoptic scales (e.g., Nitta 1987; Kawamura et al. 1996; Zhu et al. 2020). SKY21 showed that the intraseasonal PJ pattern has a statistically significant relationship with BSISO migration, indicating that the positive PJ pattern is most active during BSISO phase 8, when active BSISO convection is located in the vicinity of the Philippines. Here and thereafter, the PJ pattern is defined to be positive if it is associated with anomalously active convection in the tropical WNP, and vice versa for the negative phase. SKY21 also showed that intraseasonal responses to the BSISO both in the tropics and midlatitudes are stronger in the positive interannual PJ years than in the negative years, exhibiting interannual modulations. Wave train signals of circulation anomalies extending from north of the Philippines toward North America are apparent during BSISO phase 7 only during the positive PJ years. Relevant studies (Li et al. 2018, 2019) have shown that the ISO during phases 6 and 7 has a large influence on the interannual PJ mode through a change in frequency.

What causes the differences in the strength and behavior of the intraseasonal PJ pattern associated with BSISO in different interannual PJ years is still an open question. While SKY21 showed that the intraseasonal positive PJ pattern became most apparent in BSISO phase 8, there was no significant correlation between the amplitude of BSISO averaged for phases 7–8 and that of the intraseasonal PJ pattern. The fact that the intraseasonal PJ pattern is phase-locked to BSISO migration but does not depend on the BSISO amplitude confirms that the intraseasonal PJ pattern and BSISO are different phenomena. Instead of the BSISO itself, shorter-scale phenomena such as synoptic-scale disturbances may influence the amplitude of the intraseasonal PJ pattern. For example, it has been indicated that TC occurrences in the tropical WNP induce an extratropical wave train pattern similar to the PJ pattern (e.g., Kawamura and Ogasawara 2006; Yamada and Kawamura 2007). This motivates us to investigate the activity of synoptic-scale disturbances embedded in the BSISO convection. This study investigates the development mechanism of synoptic-scale disturbances over the tropical WNP associated with the BSISO during the different interannual PJ years.

The rest of this paper is organized as follows. The datasets and methodology are described in Section 2. Intraseasonal signals associated with the BSISO under the different PJ years are shown in Section 3. Section 4 provides the results of the eddy kinetic energy budget focusing on synoptic-scale disturbances associated with the BSISO. In Section 5, we examine the environmental fields leading to the development of synoptic disturbances. The final section provides a summary and discussion.

2. Data and methodology

The Japanese 55-year reanalysis data (JRA55; Kobayashi et al. 2015) provided by the Japan Meteorological Agency for the 1979–2018 period are used. Daily mean data of zonal and meridional winds (*u* and *v*, respectively), pressure vertical velocity ω, temperature *T*, and geopotential Φ at pressure (p) levels from 1000 to 100 hPa were derived from 6-hourly data with a horizontal resolution of 1.25°. Daily outgoing longwave radiation (OLR) data compiled by the U. S. National Oceanic and Atmospheric Administration (NOAA) on a 2.5° × 2.5° grid (Liebmann and Smith 1996) are used as a measure of convective activities. In addition, daily optimum interpolation SST high-resolution dataset (version 2.1), provided by the NOAA/National Centers for Environmental Information (NCEI), on a 0.25° × 0.25° grid (e.g., Reynolds et al. 2007; Huang et al. 2020) for 1982–2018 is used. To extract intraseasonal anomalies, a 91-day running-mean daily climatology of the annual cycle is first removed, and then a 20–100-day bandpass filter is applied to all data.

Information on TCs in the WNP and the South China Sea are provided by the Regional Specialized Meteorological Center (RSMC) Tokyo. The positions and intensities of TCs every 6 hours are derived from RSMC best-track data for 1979–2018. In this study, we consider only TCs that had intensities greater than or equal to a tropical depression and calculate the daily TC occurrence frequency on a 5° × 5° grid, which is defined as the number of TCs centered within each grid box in the 6-hourly data averaged per day. For example, the TC occurrence frequency is 1 if a TC is located in one grid box for 24 hours.

An empirical orthogonal function (EOF) analysis is applied to summer (June–August, JJA) mean data of horizontally smoothed vorticity at 850 hPa over the WNP region (0°–60°N, 100°E–160°E) to obtain the interannual PJ pattern. The standardized time series of the leading principal component, with a variance fraction of 30.2%, is used as the interannual

PJ pattern index in this study. Positive (negative) PJ years are detected when the PJ index is higher (lower) than +0.8 (–0.8), as in SKY21. Note that the positive PJ pattern represents cyclonic and anticyclonic circulation anomalies in the tropical and midlatitude lobes, respectively. The residual years are categorized into the non-PJ years. The 8 positive (9 negative) PJ years detected in this study are 1985, 1986, 1990, 1997, 2001, 2002, 2004, and 2018 (1980, 1983, 1988, 1995, 1996, 1998, 2008, 2013, and 2017). Since negative PJ years have been observed more frequently in post-El Niño summers (e.g., Xie et al. 2009, 2016), we check their relationship with ENSO. Referring to the ENSO warm and cold episode data based on a threshold of +/–0.5 °C of three month running mean SST anomalies in the Niño 3.4 region provided by NOAA/Climate Prediction Center (CPC), five-eighths of the positive PJ years are found in the concurrent El Niño years; that is, JJA preceding the El Niño peak usually in boreal winter. Three-eighths of the positive years correspond to post-La Niña years. Regarding the negative PJ years, six (five)-ninths are observed in concurrent La Niña (post-El Niño) years. The summers of concurrent ENSO correspond better to the PJ years than the summers of post-ENSO. Considering the rate of correspondence with El Niño and La Niña years, 63% and 67% in the positive and negative PJ years, respectively, ENSO is suggested to play a major role for the formation of the interannual PJ pattern, but other factors are also likely to have a contribution.

We adopt the BSISO index proposed by Kikuchi et al. (2012) based on the extended EOF analysis of intraseasonal OLR variability during boreal summer. A BSISO event in this study is identified when the amplitude of the BSISO index exceeds 1.0 for 15 consecutive days during boreal summer (JJA). As already mentioned in SKY21, the difference is negligible in the average number of BSISO events among the positive PJ, negative PJ, and non-PJ years.

3. Intraseasonal BSISO signals associated with the interannual PJ pattern

Figure 1 compares composite intraseasonal OLR and 850 hPa wind anomalies for the BSISO events (starting from phase 4) during the negative, positive, and non-PJ years. Hereafter, the statistical significance of composite results is examined using Student's t test. The effective degree of freedom is defined as the number of samples divided by the average duration in each BSISO phase. While organized convection associated with the BSISO generally migrates northeastward from the Maritime Continent to the Philippine Sea from phases 4 to 8, a drastic enhancement of convection with cyclonic anomalies over the western Pacific appears only in the positive PJ years from phases 5 to 7. In our previous study (SKY21), wave train signals extending from the vicinity of the Philippines toward North America were found only during the positive PJ years in association with the enhanced convection over the Philippine Sea. During the negative PJ years, by contrast, intraseasonal convection is intensified mainly over the South China Sea. The non-PJ years show mixed features of the negative and positive PJ years. These results indicate that there are differences in the areas of localized convective intensification even within the large-scale convective envelope among the identified BSISO cases. Active convection in the convective envelope can be associated with the passage of vigorous synoptic-scale disturbances. Considering the lack of significant correlation between the amplitude of BSISO during phases 7–8 and that of the intraseasonal PJ pattern (SKY21), the behavior of internal synoptic-scale disturbances within the BSISO convective envelope may cause the differences. Therefore, the present study focuses on the activity of synoptic-scale disturbances associated with the BSISO.

4. Energetics associated with the BSISO

To isolate the synoptic disturbances, all variables are decomposed into mean and eddy components. The mean components represented with an overbar are defined as an 11-day running mean, which represents intraseasonal time scales and longer. A prime indicates the eddy components with periods shorter than intraseasonal time scales, which are defined as deviations from the 11-day running mean.

Figure 2 depicts composite eddy kinetic energy (*K'*) at 850 hPa and convectively active regions of the BSISO represented by red contours for the BSISO events. Here, *K'* is defined as

$$K' = \frac{1}{2}(\overline{u'^2} + \overline{v'^2}) \quad . \qquad (1)$$

The *K'* values start to increase in and to the north of the BSISO convective envelope over the WNP from BSISO phase 5. From phases 6 to 7, drastic enhancement of synoptic disturbances represented by *K'* is observed widely over the Philippine Sea during the positive PJ years, whereas the disturbances are weak and confined to the north of the Philippines in the negative PJ years. Moderately active disturbances are found but confined west of 130°E in the non-PJ years. It is interesting to note that only during the positive PJ years do high *K'* values extend further east and reach approximately 150°E in phase 7, although the BSISO convection spreads to 160°E both in the positive and non-PJ years. Apparent differences in the location of active synoptic disturbances in the same BSISO phase among the three groups may explain an important part of the different midlatitude responses found in SKY21.

The distributions of high *K'* values resemble those of tropical cyclone occurrence averaged for phases 6–8 (Fig. 3). TC occurrence is most frequent over the Philippine Sea between 15°N and 25°N and extend eastward to 150°E during the positive PJ years, while it is less frequent and found mainly over the South China Sea in the negative PJ years. In the non-PJ years, frequent TC occurrences are observed both over the South China Sea and Philippine Sea. A comparison for the positive PJ and non-PJ years shows that frequent TC areas over the WNP retreat westward in the non-PJ years than in the positive PJ years. These results indicate that environmental fields in the negative PJ, positive PJ, and non-PJ years are favorable for the development of synoptic disturbances over the South China Sea, the Philippine Sea, and both, respectively, leading to differences in the TC occurrence areas. The eastward and westward shifts of frequent TC regions over the WNP in the positive and negative PJ years, respectively, are similar to the eastward/southeastward displacement of the TC genesis region in El Niño years compared with La Niña years (e.g., Wang and Chan 2002; Camargo and Sobel 2005). Further studies are needed to clarify the difference in *K’* and TC distributions between ENSO and interannual PJ variability since there is a moderate relationship between the interannual PJ pattern and concurrent ENSO, as mentioned in Section 2.

To investigate the mechanism of synoptic-scale eddy development, eddy kinetic energy budget analysis is performed. The eddy kinetic energy equation is the same as that in previous studies (Seiki and Takayabu 2007; Seiki et al. 2018, 2021a) and is written as

$$\frac{\partial K'}{\partial t} = -\overline{V'_h\left(V' \cdot \nabla\right)\bar{V}_h} - \bar{V} \cdot \nabla\overline{K'} - \overline{V' \cdot \nabla K'} - \frac{R}{p}\overline{\omega' T'} - \nabla \cdot \left(\overline{V'\Phi'}\right) + D, \quad (2)$$

KmKe AmKe AeKe PeKe GKe D

where ***V*** is the three-dimensional velocity vector, $\boldsymbol{V}_h$ is the horizontal velocity vector, and *R* is the gas constant for dry air. The first term on the right-hand side denotes the barotropic energy conversion to *K’* from the mean kinetic energy (KmKe). The second and third terms indicate the advection of *K’* by the mean flow (AmKe) and the eddy flow (AeKe), respectively. The fourth term represents the conversion from eddy available potential energy to *K’* through the rising or sinking motion of warm or cold air parcels (PeKe), which is related to eddy convective activities with latent heat release by precipitation. The fifth term corresponds to the divergence of the eddy geopotential flux (GKe). The residuals described by the last term (D) represent subgrid-scale effects, dissipation, and imbalance components. Note that the terms AmKe, AeKe, and GKe are not considered real sources or sinks since they mainly represent the redistribution of energy.

Figure 4 shows the vertical structures of each composite term during BSISO phase 7 averaged over the Philippine Sea area (120°E–140°E, 10°N–25°N) for all BSISO events. Significant high *K'* generation by PeKe found in the upper troposphere at 250 hPa corresponds to diabatic heating due to precipitation caused by developed eddy convection. Then, the *K'* in the upper troposphere is redistributed into the boundary layer by GKe. Since part of GKe consists of negative PeKe mathematically, the vertical profile of GKe around 250 hPa is similar to that of PeKe with a reversed sign. The KmKe also contributes to the *K'* increase in the lower troposphere. Strong dissipation by D is apparent in the boundary layer, suggesting that *K'* is transferred from the atmosphere to the ocean due to developed synoptic-scale disturbances. The dominant terms PeKe, GKe, KmKe, and D are consistent with the results of previous studies investigating synoptic-scale disturbances in the tropics (e.g., Maloney and Dickinson 2003; Seiki and Takayabu 2007). Compared to previous studies that focus on synoptic disturbances over the tropical central Pacific and eastern Indian Ocean (Seiki et al. 2018, 2021a), the PeKe and GKe values in Fig. 4 are approximately three times larger, while the KmKe values are comparable. This comparison indicates that the *K'* generation by synoptic-scale convection over the Philippine Sea makes a larger contribution to the total *K'* increase than those in other tropical areas. Moreover, the fact that the decrease in *K'* by AmKe is not negligible and statistically significant in the lower troposphere is unique to the disturbances over the Philippine Sea. Note that the significance tests are based on deviations from climatological means from June to August of each term (see supplemental Figure 1), which are not zero, so large composite values are not necessarily statistically significant.

Horizontal distributions of composite PeKe at 250 hPa for the BSISO events are shown in Fig. 5. The contours indicate the composite tendency of K' ($\mathrm{d}K'/\mathrm{dt}$) at 850 hPa. The highest values of PeKe spread widely over the tropical WNP from 120°E to 160°E in the positive PJ years whereas they are confined west of 130°E in the non-PJ years. While the regions of high PeKe and $\mathrm{d}K'/\mathrm{dt}$ are generally coincident from phases 4 to 6, they start to be misaligned from phase 7. These results indicate that the contribution from factors other than PeKe to the development of synoptic disturbances increases from phase 7. In the negative PJ years, the large K' generation by PeKe is observed mainly in the South China Sea, consistent with the K' distribution.

The vertical component of GKe at 850 hPa is also shown in Fig. 6 to confirm whether K' in the upper troposphere primarily generated by PeKe is redistributed to the lower troposphere. The distribution of GKe at 850 hPa corresponds to that of PeKe at 250 hPa over the tropical WNP, confirming the vertical transport of PeKe by GKe. The GKe and PeKe are less consistent over land in eastern Eurasia and north of 30°N, suggesting that there are different mechanisms for the development of synoptic-scale disturbances over land and in the midlatitudes from those over tropical oceans. Note that some areas with large PeKe and GKe values are not statistically significant probably due to large variance of composite results and high climatological values.

For the composite results of KmKe at 850 hPa (Fig. 7), differences in the zonal extent of high KmKe distributions resemble that of PeKe. Statistically significant high KmKe values are located widely over the tropical WNP in the positive PJ years, concentrated in the South China Sea in the negative PJ years, and confined to the west of 140°E in the non-PJ years. Moreover, high values of KmKe are mainly observed between 10°N and 20°N, which is farther south compared with those of PeKe. These results suggest that the contribution of KmKe to the development of synoptic disturbances is confined to the early stage of development since these disturbances tend to propagate northwestward (e.g. Takayabu and Nitta 1993) and leave this latitudinal band in the midst of their development. The discrepancy between the distributions of d*K'*/dt and the *K'* generation terms (PeKe and KmKe) after convective development over the western Pacific in phase 6 is explained by the advection term AmKe (Fig. 8). Especially in the positive PJ and non-PJ years, *K'* is advected from south of 20°N to north of 20°N by the mean flow for phases 6–8 and 1, as will be shown in detail in the next section. Thus, the large *K'* in the lower troposphere produced by PeKe and KmKe in the tropics is advected to the subtropics by AmKe.

5. Relationship between synoptic disturbances and environmental fields

Since the development of tropical convection, which can lead to the PeKe increase, is facilitated over SST above 27 °C–28 °C (e.g., Gadgil et al. 1984; Graham and Barnett 1987;

Tompkins 2001) with wind convergence in the boundary layer, we examine seasonal mean SST distributions (Fig. 9). The SST values are broadly high above 29 °C from the South China Sea to the tropical western Pacific at approximately 160°E in the negative PJ years, whereas they are below 29 °C in most of the WNP in the positive PJ years. The difference suggests that the seasonal mean SST anomaly is an outcome, not a cause, of convective development because developed convection with strong winds shades insolation and enhances evaporation and ocean mixing, leading to a decrease in SST (Wang et al. 2005; Kosaka and Nakamura 2006). In addition, oceanic variability at interannual time scales, such as ENSO, can affect the seasonal mean SST values. Note that SST in the positive PJ years exceeds 28 °C broadly in the tropical WNP, which is sufficient for convection to develop, although it is the lowest among the three groups.

Meanwhile, composite intraseasonal SST anomalies (Fig. 10) show vastly different features from seasonal mean SST. During phases 3–4, strong SST warming is observed in the Philippine Sea and the South China Sea in the positive and negative PJ years, respectively. The warming appears to be associated with strong convective suppression of the BSISO over the WNP (see Fig. 1). The strongest suppression is observed over the South China Sea during phase 3 in the negative PJ years whereas convective activities are suppressed over a broad region in the WNP in the positive PJ years. In the non-PJ years, the convectively suppressed area is confined to 110°E–140°E, consistent with the SST warming area retreating westward compared with that in the positive PJ years. The high *K'* generation (contours in Fig. 10) in the early stage of convective development (phases 5–6) follows the strong warming in SST during the convectively suppressed period (phases 3–4), which suggests that the intraseasonal SST warming associated with the BSISO contributes to the development of synoptic convection (PeKe), leading to the *K’* increase. As mentioned in Introduction, the intraseasonal SST warming in the BSISO suppressed phases has been indicated to be one of the factors facilitating the activation of convection, leading to the organization of ISO convection (e.g., Hendon and Glick 1997). The SST cooling during the mature stage of convective development (phases 7–8) is probably due to reduced insolation and enhanced latent heat flux by strong winds caused by organized convection. Since seasonal mean SST in the tropical WNP is sufficiently high for convective development in all three groups (Fig. 9), shorter-scale fluctuations (Fig. 10) are suggested to be important for local convective development.

Next, we examine the contribution of intraseasonal and seasonal-mean winds to the *K’* generation through barotropic energy conversion (KmKe) and advection by the mean flow (AmKe). As shown in Fig. 4, KmKe has the second largest contribution to *K’* generation in the lower troposphere, after GKe that redistributes PeKe. The KmKe values are governed by convergence or shear of mean horizontal winds and the existence of eddies. We decompose the mean winds into intraseasonal (ISO) and low-frequency (LF) components since both components are included in the mean winds in the *K’* budget analysis (2). As a result, the two terms KmKe and AmKe, including the mean components, in (2) are decomposed as

$$-\overline{V'_h (V' \cdot \nabla)\bar{V}_h} = -\overline{V'_h (V' \cdot \nabla)\left(\bar{\bar{V}} + \tilde{V}\right)_h}, \tag{3}$$

$$-\bar{V} \cdot \nabla\overline{K'} = -\left(\bar{\bar{V}} + \tilde{V}\right) \cdot \nabla\overline{K'}, \tag{4}$$

where a double overbar denotes the LF components defined as a 60-day running mean, which represent seasonal time scales and longer, and a tilde indicates the ISO components defined as 20–100-day bandpass filtered data as described in section 2.

Figure 11 shows the vertical structures of KmKe and AmKe in which the mean components are decomposed into LF (solid) and ISO (dashed) from 1000 to 500 hPa during BSISO phases 3, 5, and 7 averaged over the Philippine Sea area (120°E–140°E, 10°N–25°N). In the positive PJ years (upper panels), the LF component of KmKe is statistically significant in the lower troposphere and two to six times larger than the intraseasonal component during the convective phases of BSISO (phases 5 and 7). Horizontal distribution of KmKe (Fig. 12) shows that the location of large positive KmKe in phase 7 is almost the same but the magnitude is different between the LF and ISO components. During the convectively suppressed phase (phase 3), the ISO component of KmKe becomes negative, showing the opposite effects between phases 3 and 7. On the other hand, the LF component substantially decreases compared to phase 7 but remains positive. Since the LF mean field does not vary at intraseasonal time scales, the decrease from phase 7 to 3 can be attributed to a weakening of eddy disturbances. These different effects by the ISO and LF components are consistent with the results regarding interactions between the BSISO and synoptic-scale disturbances in boreal summer (Hsu et al. 2011; Tsou et al. 2014). Regarding AmKe (yellow lines in Fig. 11) in the positive PJ years, the negative effect of the LF component is much larger than that of the ISO component in phases 3 and 5, and they are comparable in phase 7, although they are statistically significant only for the LF component in phase 7. These results indicate that large *K'* values are mostly advected by the LF mean winds, although the ISO winds make an equal contribution to the advection only in phase 7.

Similar features in the vertical structures of KmKe and AmKe are also found in the non-PJ years but their intensity is smaller than that in the positive PJ years. In the negative PJ years (lower panels in Fig. 11), the total values of both terms averaged over the WNP are smaller than those in the positive PJ years like *K'*. Differences between the LF and ISO components are small and not statistically significant.

The fact that the KmKe and AmKe values converted from ISO mean fields are comparable among the three groups indicates that the BSISO wind fields exhibit small interannual variability. Overall, the LF components contribute to the *K'* increase more than the ISO components.

To unravel the larger contribution of low-frequency components, seasonal-mean and intraseasonal wind patterns are compared (Fig. 13). Seasonal mean wind patterns averaged for JJA show that the eastward extension of monsoon westerlies is strongest (weakest) in the positive (negative) PJ years (Fig. 13, left). Strong meridional and zonal gradients of seasonal mean zonal winds extending from northwest to southeast over the WNP correspond to the large KmKe areas during phases 5–8 shown in Fig. 6. Figure 13 also shows that the intensity of seasonal mean winds at 850 hPa is twice as large as intraseasonal wind anomalies averaged from BSISO phase 6 to 8 (note the difference color bars between the left and right panels). Considering stronger horizontal gradients of seasonal-mean winds, the contribution to the KmKe from seasonal-mean wind pattern is found to be overall larger than that from intraseasonal wind pattern, consistent with the results in Fig. 11. In addition, the differences between the positive and negative PJ years, positive and non-PJ years, and non-PJ and negative PJ years are larger in the interannual components than in the intraseasonal ones (Fig. 14), indicating that interannual components primarily contribute to the differences. Indeed, much stronger monsoon westerlies are found over the WNP in the positive PJ years than in the negative years (Fig. 14, upper), whereas the differences in intraseasonal wind anomalies (Fig. 14, right) are generally small. This contrast is consistent with the KmKe values shown in Fig. 11. Especially, the difference in intraseasonal anomalies between the positive and non-PJ years is negligible over the WNP. Thus, the strength of intraseasonal wind anomalies associated with the BSISO are less dependent on interannual variability.

In summary, distributions of intraseasonal SST anomalies during the convectively suppressed phases of the BSISO and seasonal-mean horizontal wind pattern in the lower troposphere associated with interannual fluctuations of monsoon westerlies are responsible for the increase in PeKe and KmKe, respectively, during the convectively active phases of the BSISO.

6. Summary and discussion

In this study, the mechanisms of synoptic-scale disturbances over the WNP associated with the BSISO under different seasonal-mean PJ conditions are examined. Our previous study (SKY21) showed the interannual modulations of the intraseasonal PJ pattern; that is, intraseasonal responses to the BSISO are stronger in the interannual positive PJ years than in the negative years, and clear wave train signals of circulation anomalies extending from the tropics to midlatitudes are found only in the positive PJ years during BSISO phase 7. In this study, a drastic development of intraseasonal convection is found widely over the tropical WNP from phases 5 to 7 in the positive PJ years, while enhanced convection is confined over the South China Sea in the negative PJ years. Considering the results in SKY21 in which the amplitude of BSISO during phases 7–8 did not correlate with that of the intraseasonal PJ pattern, differences in the areas of localized convective intensification within the large-scale convective envelope of the BSISO over the WNP may be attributed to the behavior of internal synoptic-scale disturbances. Therefore, in this study, we focus on the activity of synoptic-scale disturbances associated with the BSISO, and a similar contrast between the positive and negative PJ years is also observed in the distributions of *K’* (the activity of synoptic disturbances) and TC occurrences. Large *K’* increases and frequent TC occurrences are found over the Philippine Sea and South China Sea in the positive and negative PJ years, respectively. These results suggest that shorter-scale phenomena such as synoptic-scale disturbances in the tropics contribute to localized convective intensification within the BSISO envelope, resulting in different behavior of the intraseasonal PJ pattern. The east–west shift in TC occurrences over the WNP is similar to the characteristics associated with warm and cold episodes of ENSO (e.g., Wang and Chan 2002). The rate of correspondence with ENSO is approximately two-third. While the large contribution from ENSO is recognized, further studies are needed to clarify factors other than ENSO.

Our *K'* budget analysis shows that synoptic convection through PeKe primarily contributes to the *K'* increase. In addition, the barotropic energy conversion, KmKe, related to mean wind fields has the second largest contribution in the lower troposphere, especially during the early stage of development. The high *K'* generated by PeKe and KmKe is advected from the tropical WNP to the subtropics by the mean southerly flow (AmKe) in the lower troposphere during the mature stage of development. Compared with previous studies using the same *K'* budget analysis over the tropical central Pacific and eastern Indian Ocean (Seiki et al. 2018, 2021a), the *K'* generation by synoptic convection (PeKe) and *K'* redistribution (GKe) are approximately three times larger, while the KmKe values are comparable. This can be attributed to the fact that the WNP, which lies in the monsoon trough over the warm pool in boreal summer, is where convection is most active. Moreover, the northward advection of *K'* by AmKe, which is statistically significant in the lower troposphere, resembles the northwestward advection of cyclonic vorticities over the monsoon trough region (e.g., Lau and Lau 1992).

High PeKe over the Philippine Sea and South China Sea in the positive and negative PJ years, respectively, may be attributed in part to different behaviors of intraseasonal SST variability associated with the BSISO. Specifically, convective suppression in the BSISO phases 1–4 warms the underlying sea surface over the WNP and South China Sea in the positive and negative PJ years, respectively, which preconditions the subsequent convection development when the active phases arrive. Then, decreased insolation and enhanced latent heat flux by strong winds cool the sea surface during the phases 5–8. During the suppressed BSISO phase, phase 3, organized active convection associated with the BSISO is located in almost the same regions from the equatorial Indian Ocean to the Maritime Continent between the positive and negative PJ years (see Fig. 1). It thus requires future studies to reveal why the intraseasonal suppressed regions appear in different locations. Large-scale ascending areas at interannual time scales may influence the different locations of the suppressed convection. Regarding KmKe, on the other hand, interannual wind fields in the lower troposphere, especially the strength of monsoon westerlies and their shear, contribute more to the high KmKe than intraseasonal wind fields. The convergence and shear areas of monsoon westerlies extend eastward (retreat westward) in the positive (negative) PJ years, resulting in high K' over the Philippine Sea (South China Sea). Southerly winds over the convergence area contribute to the northward advection of synoptic disturbances through AmKe. The KmKe and AmKe converted from intraseasonal mean fields are comparable between the positive and negative PJ years, indicating that the BSISO wind fields exhibit small interannual variability.

Although we focused only on the tropical forcing associated with atmospheric convection to the PJ pattern, variability in the background wind fields at midlatitudes, such as the westerly jet, may be another factor for different PJ signals responding to the forcing (e.g., Kosaka and Nakamura 2010; Ye and Lu 2011). Previous studies have indicated an influence of the PJ pattern on TC tracks in the subtropics and midlatitudes (e.g., Choi et al. 2010). Detailed studies are needed to clarify the interacting relationship between tropical forcing, such as organized convection, and the PJ pattern across the tropics and midlatitudes.

Data Availability Statement

The JRA55 data are available through the Japan Meteorological Agency (https://jra.kishou.go.jp/JRA-55/index_en.html). The OLR data are derived by NOAA (https://psl.noaa.gov/data/gridded/data.interp_OLR.html). The SST dataset can be obtained from the NOAA/NCEI (https://www.ncei.noaa.gov/products/optimum-interpolation-sst). Data on the positions and intensities of TCs are provided by the RSMC Tokyo (https://www.jma.go.jp/jma/jma-eng/jma-center/rsmc-hp-pub-eg/besttrack.html). The ENSO warm and cold episode data are available at NOAA/CPC (https://origin.cpc.ncep.noaa.gov/products/analysis_monitoring/ensostuff/ONI_v5.php). The

BSISO index is available at (http://iprc.soest.hawaii.edu/users/kazuyosh/Bimodal_ISO.html).

Supplement

Supplement 1 shows the climatological means of (a) PeKe at 250 hPa, (b) KmKe, and (c) VbKe at 850 hPa (10^{-5} m^2 s^{-3}) for June–August.

Acknowledgments

This study is supported by Japan Society for the Promotion of Science through Grants-in-Aid for Scientific Research (JP18H05879, JP19K21060, JP18H01278, JP19H05703, JP20H01386, JP20H02252, and JP20H05730), by the Environmental Restoration and Conservation Agency of Japan through the Environmental Research and Technology Development Fund (JPMEERF20192004 and JPMEERF20222002), and by the Japanese Ministry of Education, Culture, Sports, Science and Technology (JPMXD0722680395).

References

Camargo, S. J., and A. H. Sobel, 2005: Western North Pacific tropical cyclone intensity and ENSO. *J. Climate*, **18**, 2996–3006.

Camargo, S. J., M. C. Wheeler, and A. H. Sobel, 2009: Diagnosis of the MJO modulation of tropical cyclogenesis using an empirical index. *J. Atmos. Sci.*, **66**, 3061–3074.

Choi, K.-S., C.-C. Wu, and E.-J. Cha, 2010: Change of tropical cyclone activity by Pacific-

Japan teleconnection pattern in the western North Pacific. *J. Geophys. Res.*, 115, D19114.

Gadgil S., P. V. Joseph, and N. V. Joshi, 1984: Ocean-atmosphere coupling over monsoon regions. *Nature*, **312**, 141–143

Graham N. E., and T. P. Barnett, 1987: Sea surface temperature, surface wind divergence, and convection over tropical oceans. *Science*, **238**, 657–659.

Hendon H. H., and J. Glick, 1997: Intraseasonal air-sea interaction in the tropical Indian and Pacific Oceans. *J. Climate*, **10**, 647–661.

Hendon, H. H., and M. L. Salby, 1994: The life cycle of the Madden-Julian oscillation. *J. Atmos. Sci.*, **51**, 2225–2237.

Hsu, P.-C., T. Li, and C.-H. Tsou, 2011: Interactions between boreal summer Intraseasonal oscillations and synoptic-scale disturbances over the western North Pacific. Part I: Energetics diagnosis. *J. Climate*, **24**, 927–941.

Huang, B., C. Liu, V. Banzon, E. Freeman, G. Graham, B. Hankins, T. Smith, and H.-M. Zhang, 2020: Improvements of the Daily Optimum Interpolation Sea Surface Temperature (DOISST) Version 2.1, *Journal of Climate*, **34**, 2923–2939.

Johnson, R. H., T. M. Rickenbach, S. A. Rutledge, P. E. Ciesielski, and W. H. Schubert, 1999: Trimodal characteristics of tropical convection. *J. Climate*, **12**, 2397–2418.

Katsumata, M., H. Yamada, H. Kubota, Q. Moteki, and R. Shirooka, 2013: Observed evolution of northward-propagating intraseasonal variation over the western Pacific: A case study in boreal early summer. *Mon. Wea. Rev.*, **141**, 690–706.

Kawamura, R., T. Murakami, and B. Wang, 1996: Tropical and mid-latitude 45-day perturbations over the western Pacific during the northern summer. *J. Meteor. Soc. Japan*, **74**, 867–890.

Kawamura, R., and T. Ogasawara, 2006: On the role of typhoons in generating PJ teleconnection patterns over the western north Pacific in late summer. *SOLA*, **2**, 0377–040.

Kemball-Cook, S. R., and B. C. Weare, 2001: The onset of convection in the Madden–Julian Oscillation. *J. Climate*, **14**, 780–793.

Kikuchi, K. 2021: The Boreal Summer Intraseasonal Oscillation (BSISO): A Review. *J. Meteor. Soc. Japan*, **99**, 933–972.

Kikuchi, K., and Y. N. Takayabu, 2004: The development of organized convection associated with the MJO during TOGA COARE IOP: Trimodal characteristics. *Geophys. Res. Lett.*, **31**, L10101.

Kikuchi, K., B. Wang, and Y. Kajikawa, 2012: Bimodal representation of the tropical intraseasonal oscillation. *Climate Dyn.*, **38**, 1989–2000.

Knutson, T. R., and K. M. Weickmann, 1987: 30-60 Day Atmospheric Oscillations: Composite Life Cycles of Convection and Circulation Anomalies. *Mon. Wea. Rev.*, **115**, 1407–1436.

Kobayashi, S., Y. Ota, Y. Harada, A. Ebita, M. Moriya, H. Onoda, K. Onogi, H. Kamahori, C. Kobayashi, H. Endo, K. Miyaoka, and K. Takahashi, 2015: The JRA-55 Reanalysis:

General Specifications and Basic Characteristics. *J. Meteor. Soc. Japan*, **93**, 5-48.

Kosaka Y., and H. Nakamura, 2006: Structure and dynamics of the summertime Pacific-Japan teleconnection pattern. *Quart. J. Roy. Meteor. Soc.*, **132**, 20097–2030.

Kosaka, Y., and H. Nakamura, 2010: Mechanisms of meridional teleconnection observed between a summer monsoon system and a subtropical anticyclone. Part I: The Pacific-Japan pattern. *J. Climate*, **23**, 50857–5108.

Kurihara, K., and T. Tsuyuki, 1987: Development of the barotropic high around Japan and its association with Rossby wave-like propagations over the North Pacific: Analysis of August 1984. *J. Meteor. Soc. Japan*, **65**, 237–246.

Lau, K.-H., and N.-C. Lau, 1992: The Energetics and Propagation Dynamics of Tropical Summertime Synoptic-Scale Disturbances. *Mon. Wea. Rev.*, **120**, 2523–2539.

Lawrence, D. M., and P. J. Webster, 2002: The boreal summer intraseasonal oscillation: relationship between northward and eastward movement of convection. *J. Atmos. Sci.*, **59**, 1593–1606.

Li X, G. Gollan, R. J. Greatbatch, and R. Lu, 2018: Intraseasonal variation of the East Asian summer monsoon associated with the Madden–Julian Oscillation. *Atmos. Sci. Lett.*, 19: e794.

Li, X., G. Gollan, R. J. Greatbatch, and R. Lu, 2019: Impact of the MJO on the interannual variation of the Pacific-Japan mode of the East Asian summer monsoon. *Climate Dyn.*, **52**, 34897–3501.

Liebmann, B., H. H. Hendon, and J. D. Glick, 1994: The relationship between tropical cyclones of the western Pacific and Indian Oceans and the Madden–Julian oscillation. *J. Meteor. Soc. Japan*, **72**, 401–412.

Liebmann, B., and C. A. Smith, 1996: Description of a Complete (Interpolated) Outgoing Longwave Radiation Dataset. *BAMS*, **77**, 1275–1277.

Madden, R. A. and P. R. Julian, 1971: Detection of a 40-50-Day Oscillation in the Zonal Wind in the Tropical Pacific. *J. Atmos. Sci.*, **28**, 702–708.

Madden, R. A. and P. R. Julian, 1972: Description of Global-Scale Circulation Cells in the Tropics with a 40-50-Day period. *J. Atmos. Sci.*, **29**, 1109–1123.

Maloney, E. D., 2009: The moist static energy budget of a composite tropical intraseasonal oscillation in a climate model. *J. Climate*, **22**, 711–729.

Maloney, E. D., and M. J. Dickinson, 2003: The Intraseasonal Oscillation and the Energetics of Summertime Tropical Western North Pacific Synoptic-Scale Disturbances. *J. Atmos. Sci.*, **60**, 2153–2168.

Maloney, E. D., and D. L. Hartrmann, 1998: Frictional moisture convergence in a composite life cycle of the Madden–Julian Oscillation. *J. Climate*, **11**, 2387–2403.

Maloney, E. D., and D. L. Hartmann, 2000: Modulation of eastern North Pacific hurricanes by the Madden–Julian oscillation. *J. Climate*, **13**, 1451–1460.

Matthews, A. J., B. J. Hoskins, and M. Masutani, 2004: The global response to tropical heating in the Madden-Julian oscillation during the northern winter. *Quart. J. Roy. Meteor.*

Soc., **130**, 1991–2011.

Nakazawa, T., 1988: Tropical Super Clusters within Intraseasonal Variations over the Western Pacific. *J. Meteor. Soc. Japan*, **66**, 823–839.

Nitta, T., 1987: Convective activities in the tropical western Pacific and their impact on the Northern Hemisphere summer circulation. *J. Meteor. Soc. Japan*, **65**, 373–390.

Reynolds, R. W., T. M. Smith, C. Liu, D. B. Chelton, K. S. Casey, and M. G. Scchlax, 2007: Daily high-resolution-blended analysis for sea surface temperature. *J. Climate*, **20**, 5473–5496.

Seiki, A., and Y. N. Takayabu, 2007: Westerly wind bursts and their relationship with intraseasonal variations and ENSO. Part II: Energetics over the western and central Pacific. *Mon. Wea. Rev.*, **133**, 3346–3361.

Seiki, A., Y. N. Takayabu, T. Hasegawa, and K. Yoneyama, 2018: Lack of westerly wind bursts in unmaterialized El Niño years. *J. Climate*, **31**, 593–612.

Seiki, A., S. Yokoi, and M. Katsumata, 2021a: The impact of diurnal precipitation over Sumatra Island, Indonesia, on synoptic disturbances and its relation to the Madden-Julian Oscillation. *J. Meteor. Soc. Japan*, **99**, 113–137.

Seiki, A., Y. Kosaka, and S. Yokoi, 2021b: Relationship between the boreal summer intraseasonal oscillation and the Pacific-Japan pattern and its interannual modulations. *SOLA*, **17**, 177–183.

Shinoda T., H. H. Hendon, and J. Glick, 1998: Intraseasonal variability of surface fluxes and sea surface temperature in the tropical western Pacific and Indian Ocean. *J. Climate*, **11**, 1685-1702.

Takayabu, Y. N., and T. Nitta, 1993: 3-5 day-period disturbances coupled with convection over the tropical Pacific Ocean. *J. Meteor. Soc. Japan*, **71**, 221–246.

Tompkins A. M., 2001: On the relationship between tropical convection and sea surface temperature. *J. Climate*, **14**, 633–637.

Tsou C.-H., H.-H. Hsu, P.-C. Hsu, 2014: The role of multi-scale interaction in synoptic-scale eddy kinetic energy over the western North Pacific in autumn. *J. Climate*, **27**, 3750–3766.

Wakabayashi, S., and R. Kawamura, 2004: Extraction of major teleconnection patterns possibly associated with the anomalous summer climate in Japan. *J. Meteor. Soc. Japan*, **82**, 1577–1588.

Wang, B., and H. Rui, 1990: Synoptic climatology of transient tropical intraseasonal convection anomalies: 1975–1985. *Meteor. Atmos. Phys.*, **44**, 43–61.

Wang, B. and J. C. L. Chan, 2002: How strong ENSO events affect tropical storm activity over the western north Pacific. *J. Climate*, **15**, 1643–1658.

Wang, B., Q. Ding, X. Fu, I.-S. Kang, K. Jin, J. Shukla, and F. Doblas-Reyes, 2005: Fundamental challenge in simulation and prediction of summer monsoon rainfall. *Geophys. Res. Lett.*, **32**, L15711, doi:10.1029/2005GL022734.

Xie, S.-P., K. Hu, J. Hafner, H. Tokinaga, Y. Du., G. huang, and T. Sampe, 2009: Indian Ocean capacitor effect on Indo-western Pacific climate during the summer following El

Niño. *J. Climate*, **22**, 730–747.

Xie, S.-P., Y. Kosaka, Y. Du, K. Hu, J. S. Chowdary, and G. Huang, 2016: Indo-western Pacific Ocean capacitor and coherent climate anomalies in post-ENSO Summer: A review. *Adv. Atmos. Sci.*, **33**, 411–432.

Yamada, K., and R. Kawamura, 2007: dynamical link between typhoon activity and the PJ teleconnection pattern from early summer to autumn as revealed by the JRA-25 reanalysis. *SOLA*, **3**, 057–068.

Ye, H. and R. Lu, 2011: Subseasonal variation in ENSO-related East Asian rainfall anomalies during summer and its role in weakening the relationship between the ENSO and summer rainfall in Eastern China since the late 1970s. *J. Climate*, **24**, 2271–2284.

Yoshida, R., Y. Kajikawa, and H. Ishikawa, 2014: Impact of boreal summer intraseasonal oscillation on environment on tropical cyclone genesis over the western north Pacific. *SOLA*, **10**, 015–018.

Zhou, C. and T. Li, 2010: Upscale feedback of tropical synoptic variability to intraseasonal oscillations through the nonlinear rectification of the surface latent heat flux. *J. Climate*, **23**, 5738–5754.

Zhu, Y., Z. Wen, Y. guo, R. Chen, X. Li, and Y. Qiao, 2020: The characteristics and possible growth mechanisms of the quasi-biweekly Pacifc-Japan teleconnection in boreal summer. *Climate Dyn.*, **55**, 33637–3380.

List of Figures

years. The dotted area represents significant PeKe with more than the 95% confidence level. Black (green) contours represent the composite positive (negative) tendency of K' (dK'/dt) at 850 hPa with intervals of 0.7 × 10^{-5} m^2 s^{-3}.

Fig. 6 The vertical component of composite GKe at 850 hPa (shading; 10^{-5} m^2 s^{-3}) for the BSISO events during phases 7 and 3 for (left) the negative PJ, (middle) positive PJ, and (right) non-PJ years. The dotted area represents significant GKe with more than the 95% confidence level. Black (green) contours represent the composite positive (negative) tendency of K' (dK'/dt) at 850 hPa with intervals of 0.7 × 10^{-5} m^2 s^{-3}.

Fig. 7 Same as Fig. 5 except for composite KmKe at 850 hPa (shading; 10^{-5} m^2 s^{-3}).

Fig. 8 Same as Fig. 5 except for composite AmKe at 850 hPa (shading; 10^{-5} m^2 s^{-3}).

Fig. 9 Seasonal mean SST averaged for JJA in (upper) the negative PJ, (middle) positive PJ, and (lower) non-PJ years (shading; ºC). Vectors indicate seasonal mean wind fields at 850 hPa (m s^{-1}).

Fig. 10 Same as Fig. 5 except for composite intraseasonal SST anomalies (shading; °C). Negative K' tendency is represented in purple.

Fig. 11 Composite vertical structures of KmKe (red) and AmKe (yellow) values (10^{-5} m^2 s^{-3}) and corresponding Student's t statistics from 1000 to 500 hPa in BSISO phases 3, 5, and 7 averaged over the Philippine Sea area (10°–25°N, 120°E–140°E) in the (upper) positive PJ, (middle) non-PJ, and (lower) negative PJ years. The dark gray vertical line in the right panels indicates the 95% confidence level. The mean components in the eddy kinetic energy budget are decomposed into LF (solid) and ISO (dashed).

Fig. 12 Composite KmKe at 850 hPa in which the mean components are decomposed into LF and ISO (shading; 10^{-5} m^2 s^{-3}) for the BSISO events during phases 7 and 3 for (left) the negative PJ, (middle) positive PJ, and (right) non-PJ years. The dotted area represents significant KmKe with more than the 95% confidence level. Black (green) contours represent the composite positive (negative) tendency of K' (dK'/dt) at 850 hPa with intervals of 0.7×10^{-5} m^2 s^{-3}.

Fig. 13 (left) Seasonal mean zonal winds at 850 hPa averaged for JJA and (right) intraseasonal zonal wind anomalies averaged from BSISO phase 6 to 8 (shading; m s^{-1}). Vectors indicate (left) seasonal mean and (right) intraseasonal wind fields at 850 hPa.

Fig. 14 Differences of (left) seasonal mean zonal winds at 850 hPa averaged for JJA and (right) intraseasonal zonal wind anomalies averaged from BSISO phase 6 to 8 (shading; m s^{-1}) between (upper) the positive and negative PJ years, (middle) positive and non-PJ years, and (lower) non-PJ and negative PJ years. Vectors indicate differences of (left) seasonal mean and (right) intraseasonal wind fields at 850 hPa.

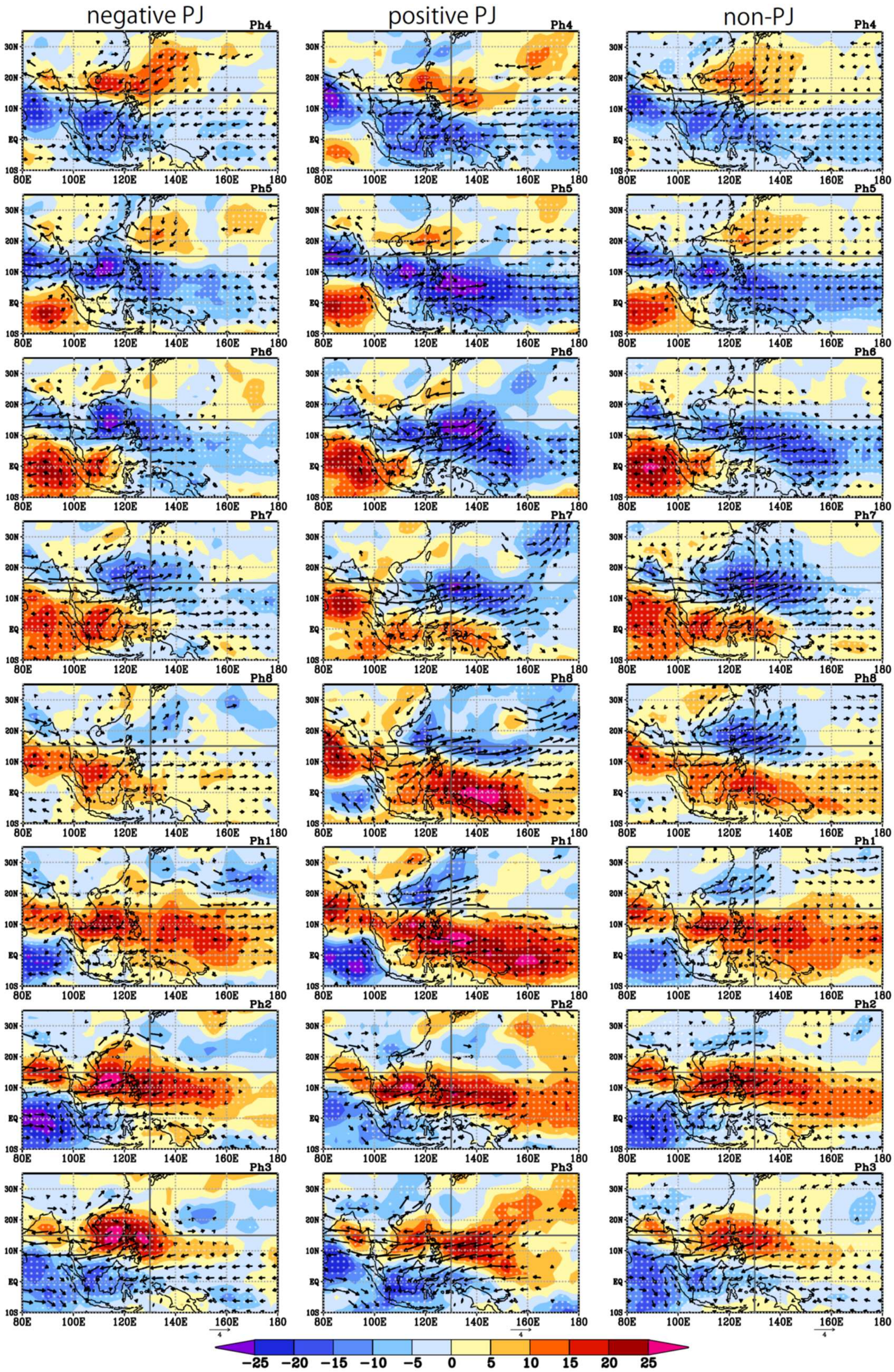

Fig. 1 Composite intraseasonal OLR anomalies (shading; W m^{-2}) for the BSISO events starting from phase 4 during (left) the negative PJ, (middle) positive PJ, and (right) non-PJ years. The dotted area represents statistical significance of more than the 95% confidence level. Vectors indicate composite wind anomaly fields at 850 hPa (ms^{-1}), where either the zonal or meridional component is significant at the 95% level.

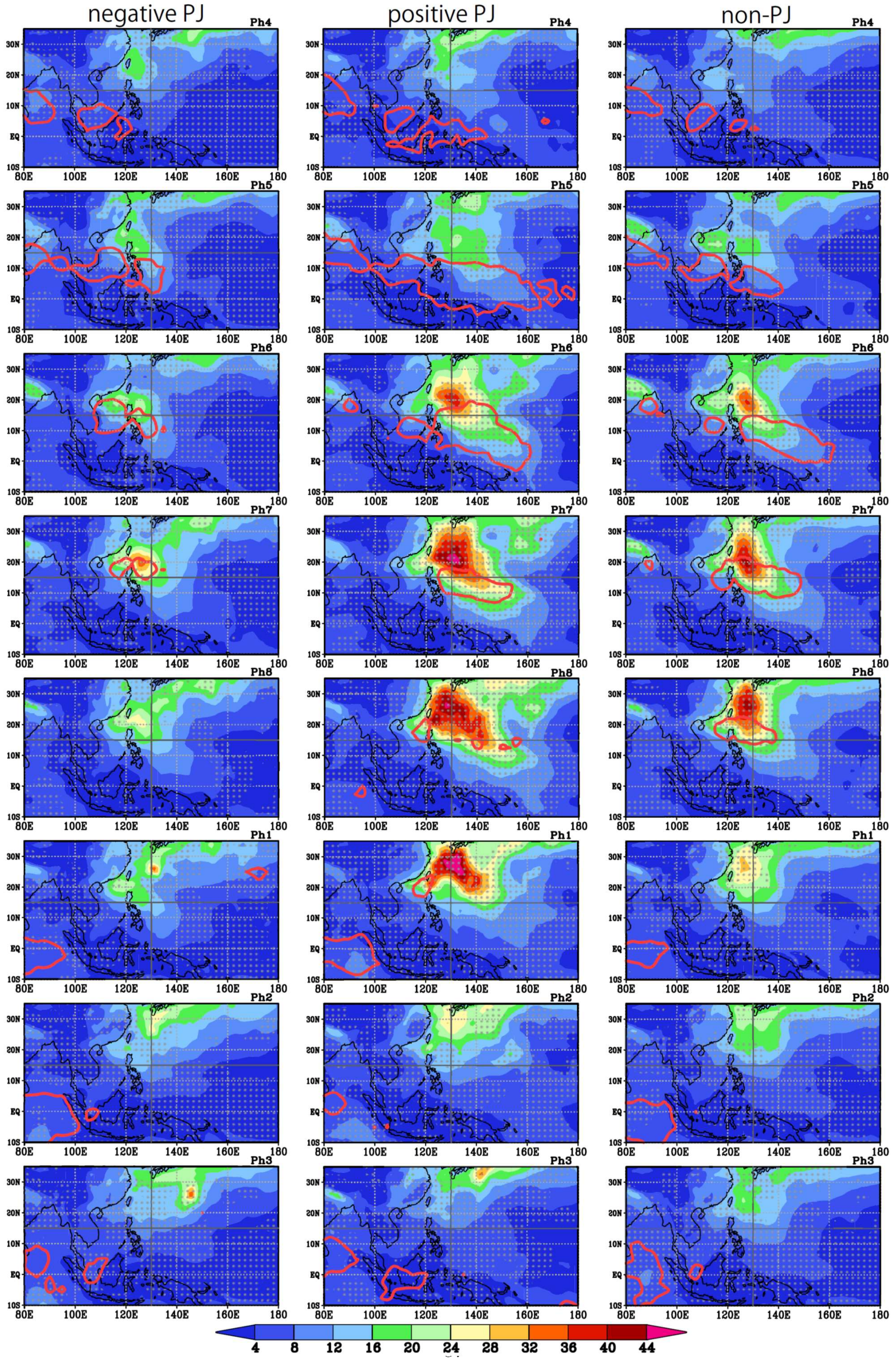
negative PJ
positive PJ
non-PJ
Ph4
Ph5
Ph6
Ph7
Ph8
Ph1
Ph2
Ph3
30N
20N
10N
EQ
10S
80E
100E
120E
140E
160E
180
4
8
12
16
20
24
28
32
36
40
44

Fig. 2 Same as Fig. 1 except for composite *K'* (shading; $m^2 s^{-2}$) at 850 hPa. The thick red contours represent composite intraseasonal OLR anomalies of –15 W m^{-2}. Note that the shading shows *K'*, not its anomaly, while the significance tests are based on anomalies from JJA climatology, which are not zero.

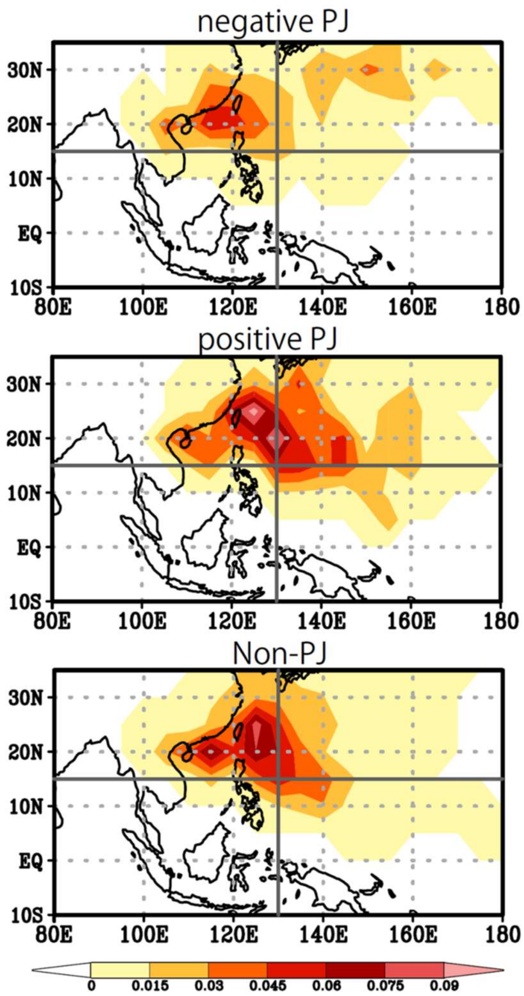

Fig. 3 Composite daily TC occurrence frequency averaged between phases 6 and 8 for the BSISO events during (upper) the negative PJ, (middle) positive PJ, and (lower) non-PJ years.

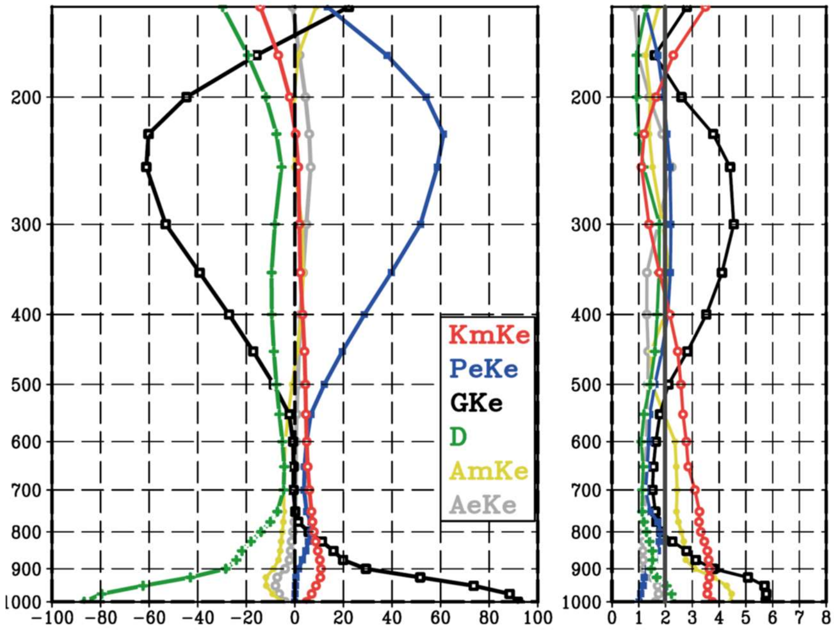

Fig. 4 (left) Composite vertical structures of each term in the eddy kinetic energy budget (10^{-5} m^2 s^{-3}) and (right) corresponding Student's t statistics from 1000 to 150 hPa for all BSISO events in phase 7 averaged over the Philippine Sea area (10°–25°N, 120°E–140°E). The dark gray vertical line in the right panel indicates the 95% confidence level.

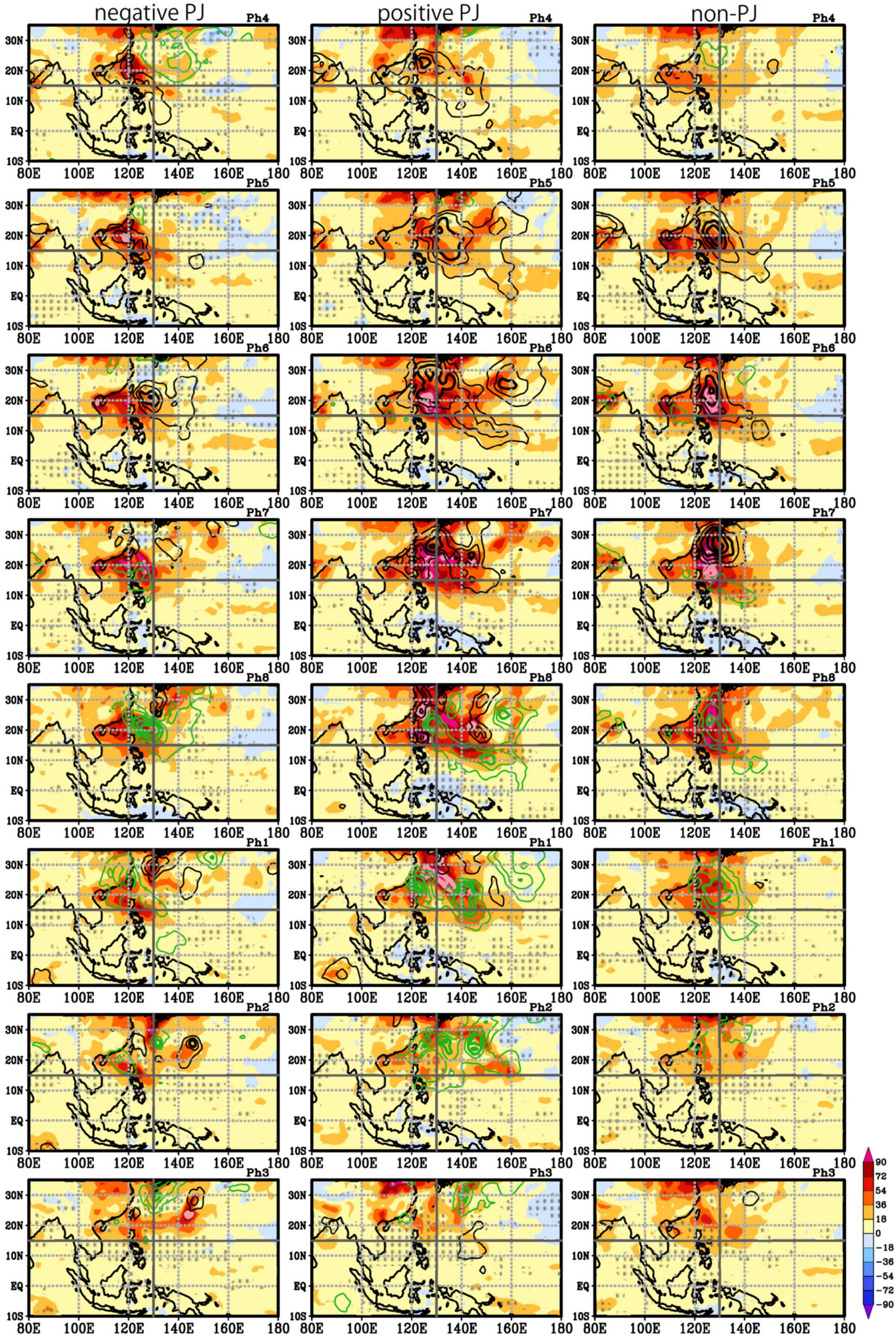

Fig. 5 Composite PeKe at 250 hPa (shading; 10^{-5} m^2 s^{-3}) for the BSISO events starting from

phase 4 during (left) the negative PJ, (middle) positive PJ, and (right) non-PJ years. The dotted area represents significant PeKe with more than the 95% confidence level. Black (green) contours represent the composite positive (negative) tendency of *K'* (d*K'*/dt) at 850 hPa with intervals of 0.7 × 10^{-5} m^2 s^{-3}.

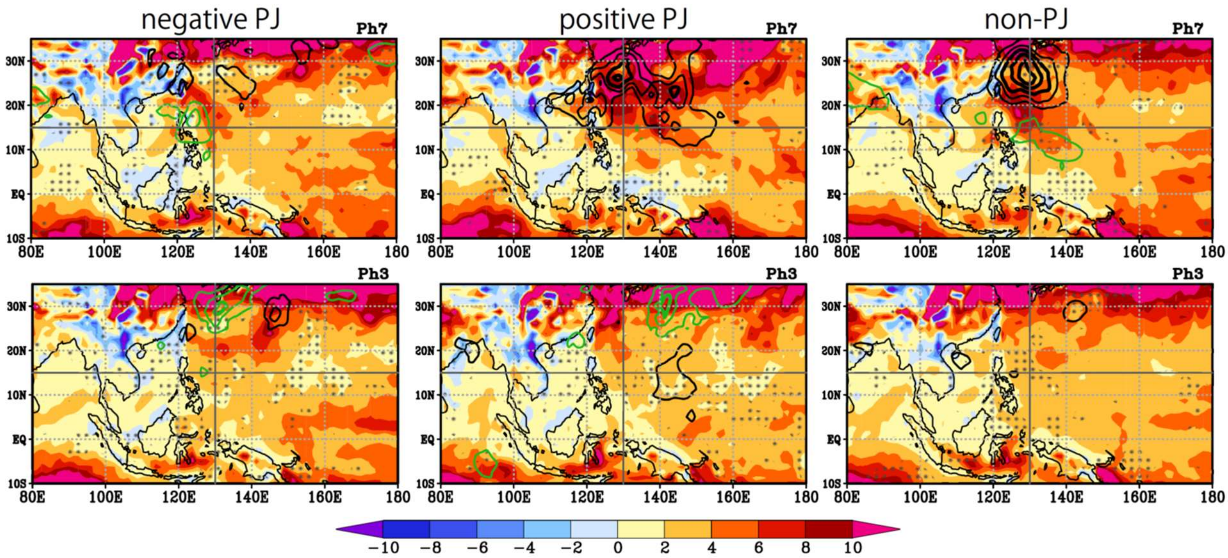

Fig. 6 The vertical component of composite GKe at 850 hPa (shading; 10^{-5} m^2 s^{-3}) for the BSISO events during phases 7 and 3 for (left) the negative PJ, (middle) positive PJ, and (right) non-PJ years. The dotted area represents significant GKe with more than the 95% confidence level. Black (green) contours represent the composite positive (negative) tendency of *K'* (d*K'*/dt) at 850 hPa with intervals of 0.7 × 10^{-5} m^2 s^{-3}.

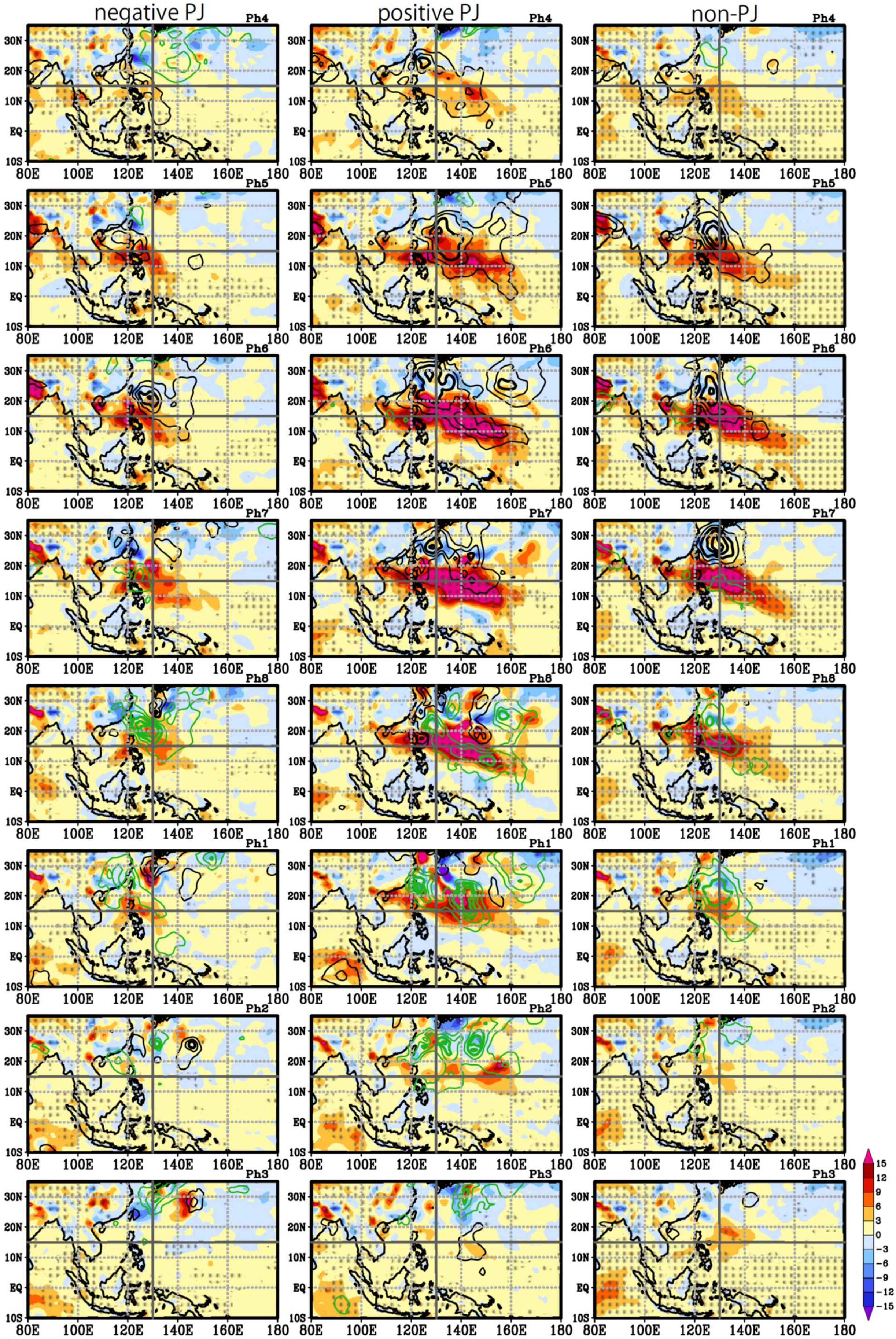

Fig. 7 Same as Fig. 5 except for composite KmKe at 850 hPa (shading; 10^{-5} m^2 s^{-3}).

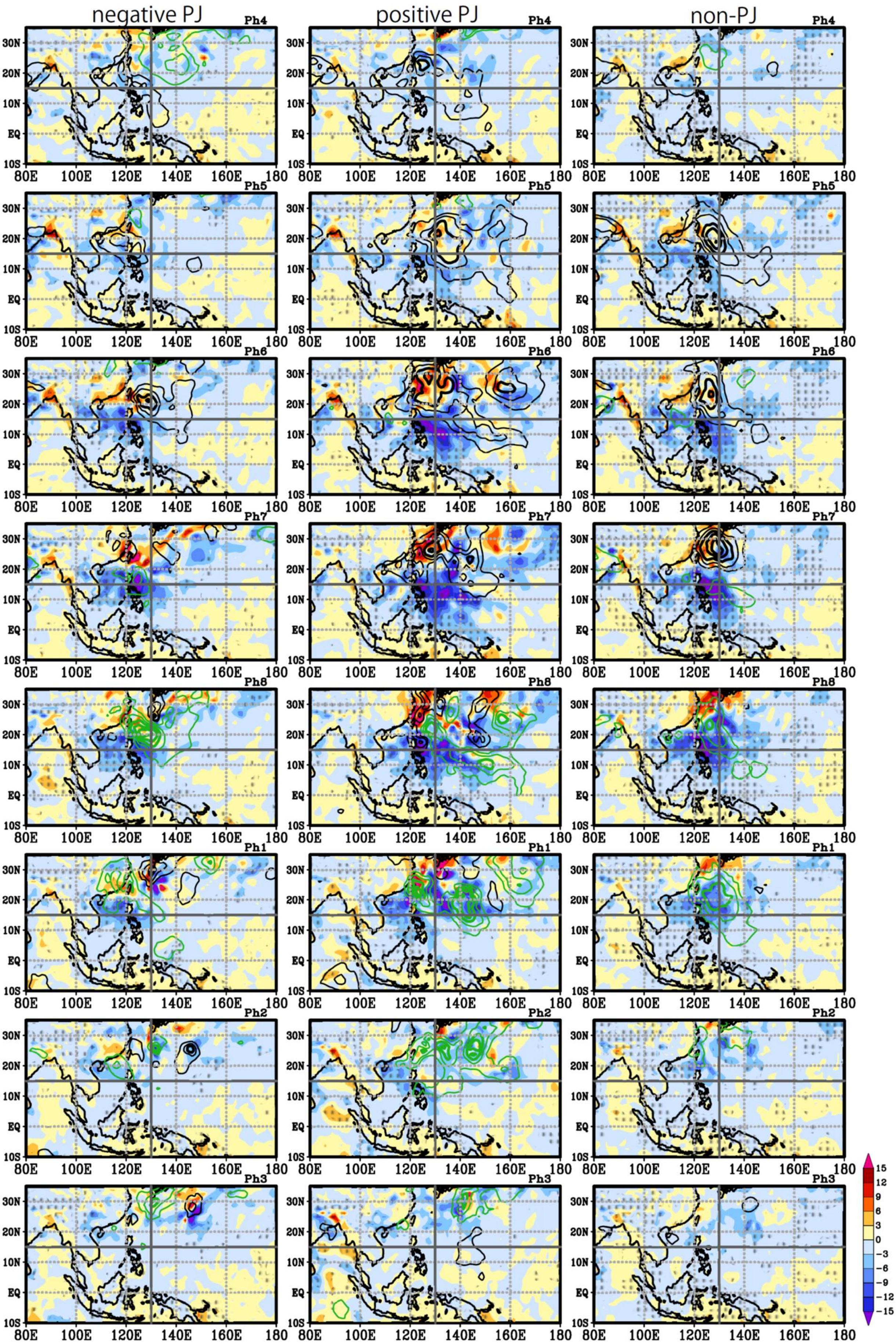

756

757 Fig. 8 Same as Fig. 5 except for composite AmKe at 850 hPa (shading; 10^{-5} m^2 s^{-3}).

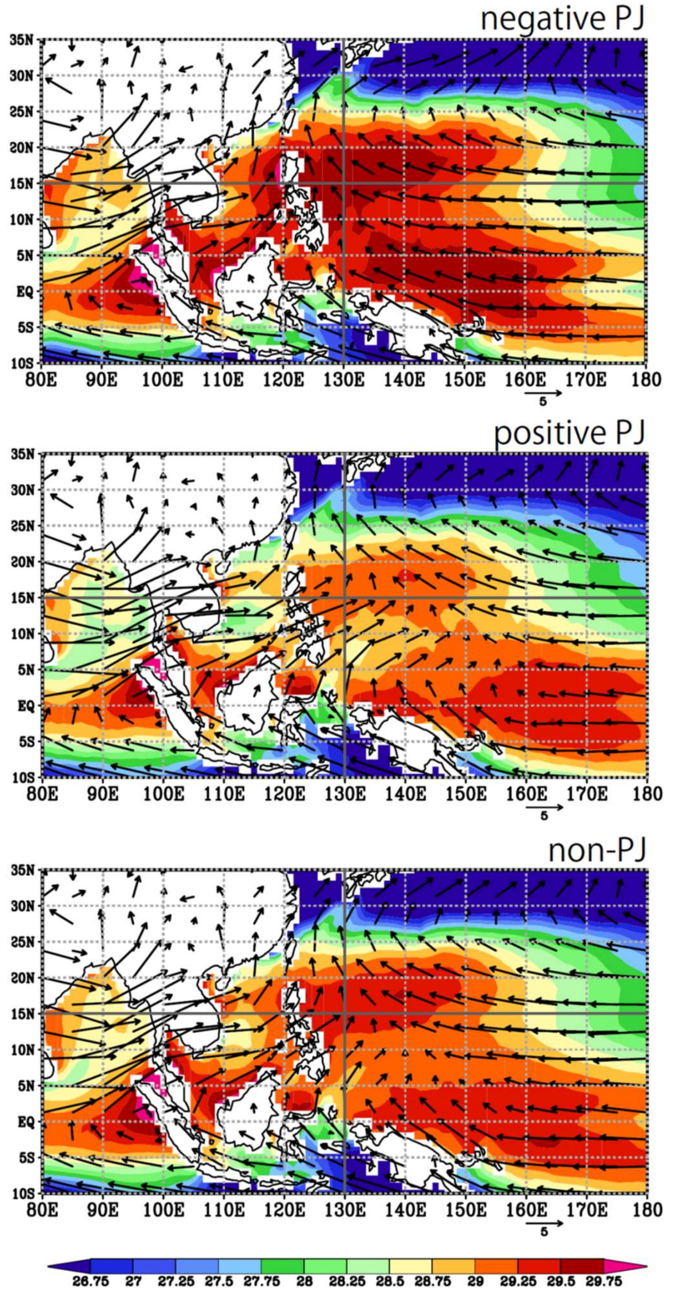

Fig. 9 Seasonal mean SST averaged for JJA in (upper) the negative PJ, (middle) positive PJ, and (lower) non-PJ years (shading; ºC). Vectors indicate seasonal mean wind fields at 850 hPa (m s^{-1}).

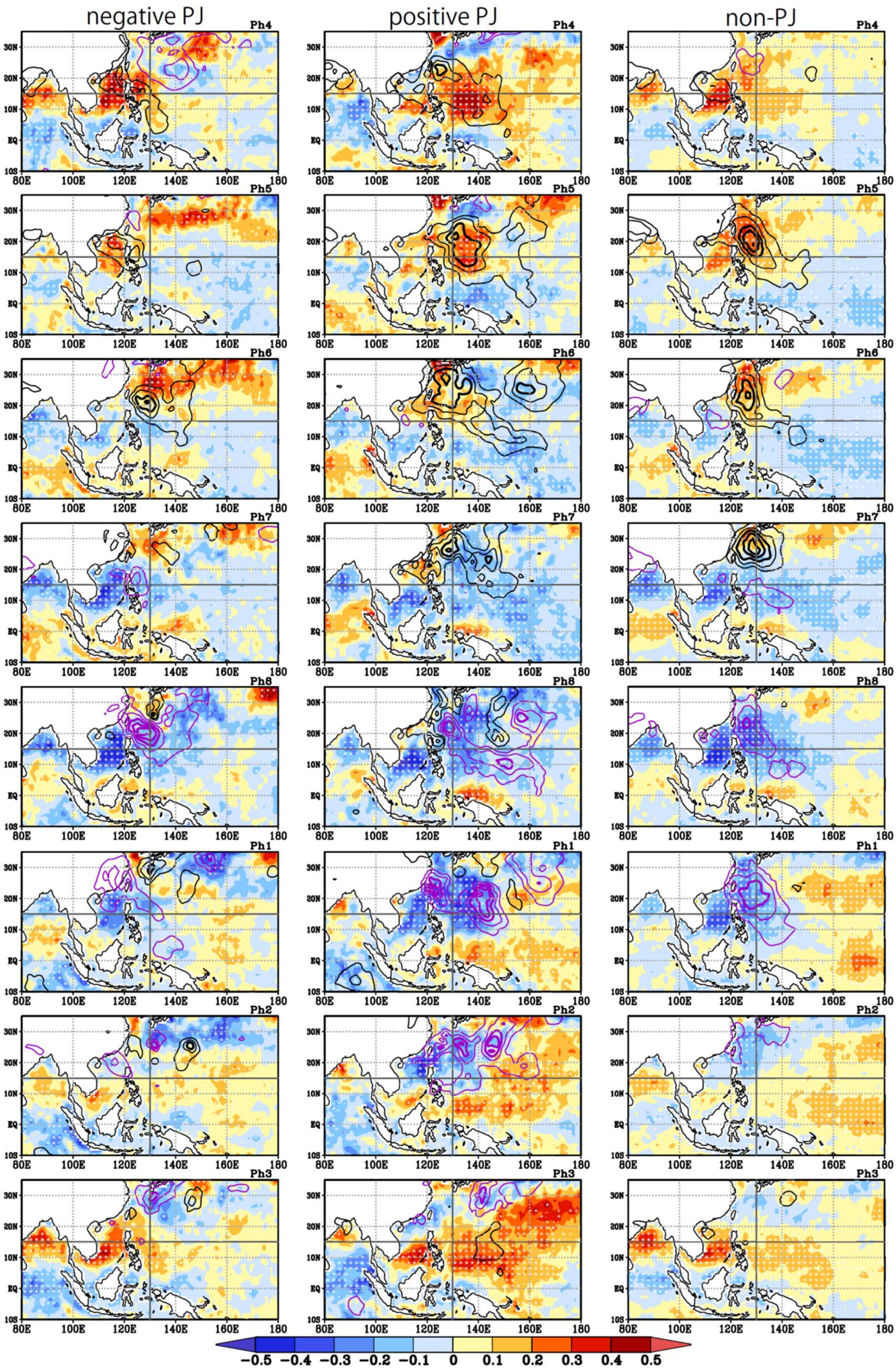

Fig. 10 Same as Fig. 5 except for composite intraseasonal SST anomalies (shading; °C). Negative *K'* tendency is represented in purple.

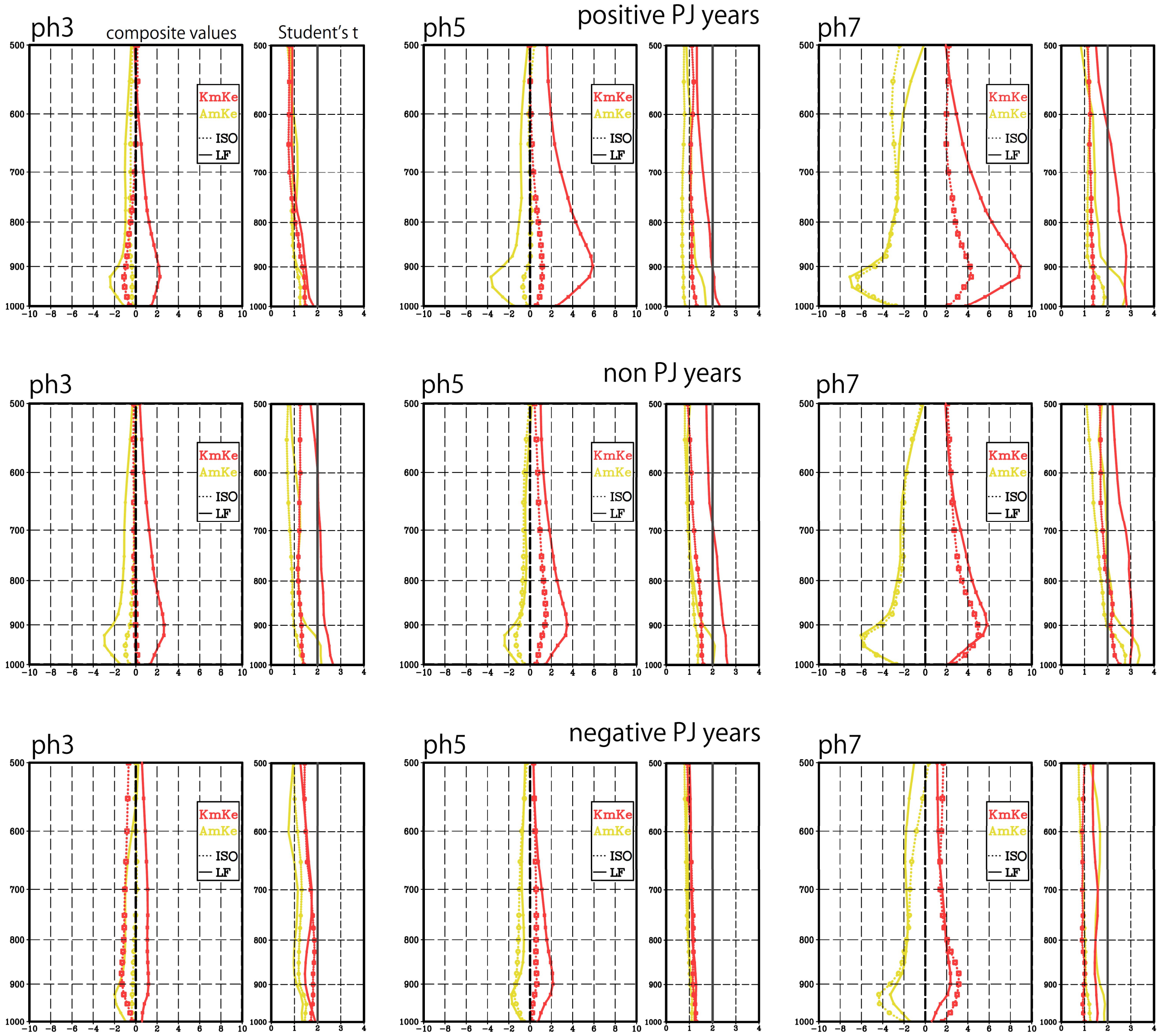

Fig. 11 Composite vertical structures of KmKe (red) and AmKe (yellow) values (10^{-5} m^2 s^{-3}) and corresponding Student's t statistics from 1000 to 500 hPa in BSISO phases 3, 5, and 7 averaged over the Philippine Sea area (10°–25°N, 120°E–140°E) in the (upper) positive PJ, (middle) non-PJ, and (lower) negative PJ years. The dark gray vertical line in the right panels indicates the 95% confidence level. The mean components in the eddy kinetic energy budget are decomposed into LF (solid) and ISO (dashed).

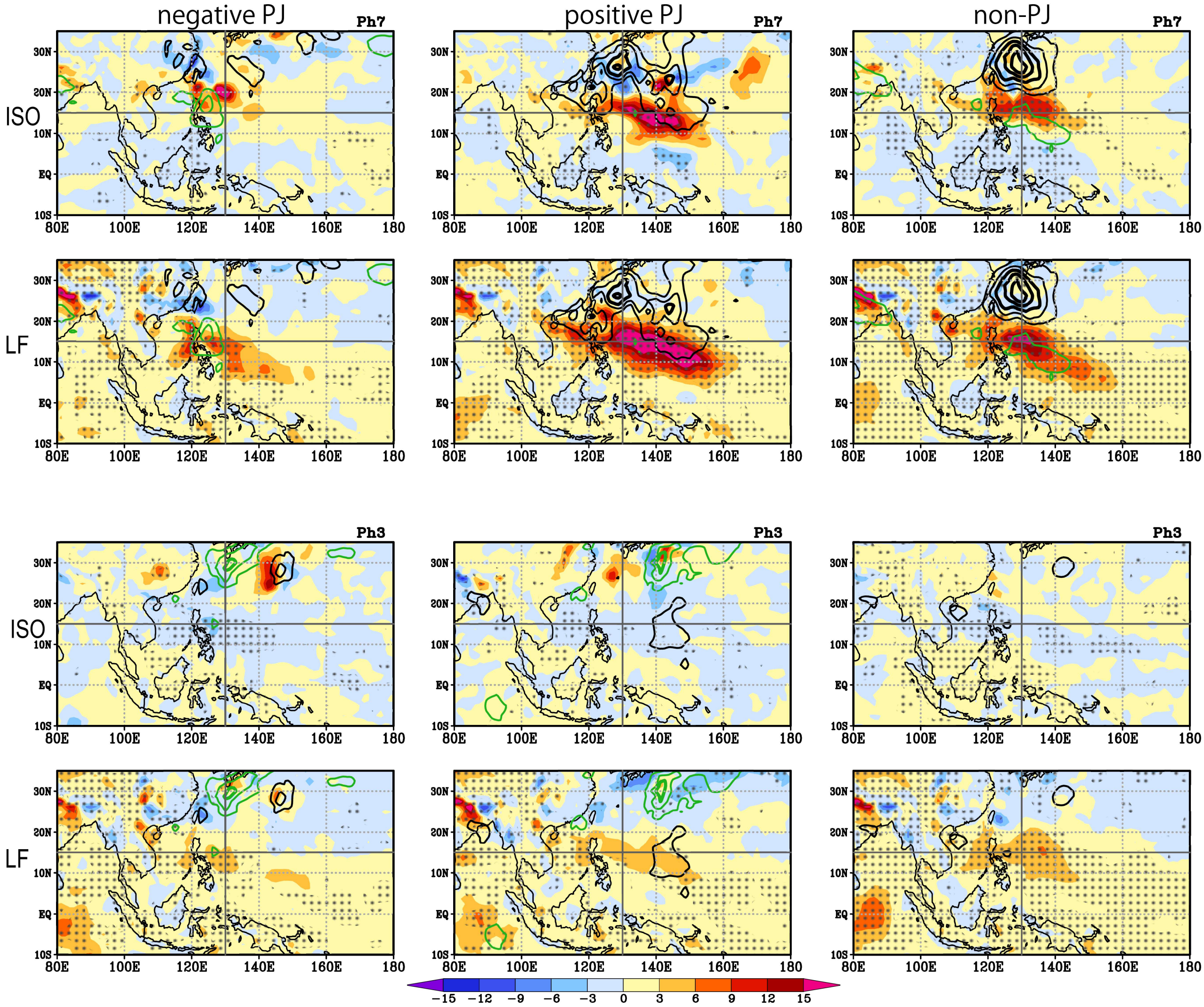

Fig. 12 Composite KmKe at 850 hPa in which the mean components are decomposed into LF and ISO (shading; 10^{-5} m^2 s^{-3}) for the BSISO events during phases 7 and 3 for (left) the negative PJ, (middle) positive PJ, and (right) non-PJ years. The dotted area represents significant KmKe with more than the 95% confidence level. Black (green) contours represent the composite positive (negative) tendency of K' (dK'/dt) at 850 hPa with intervals of 0.7 $\times$ 10^{-5} m^2 s^{-3}.

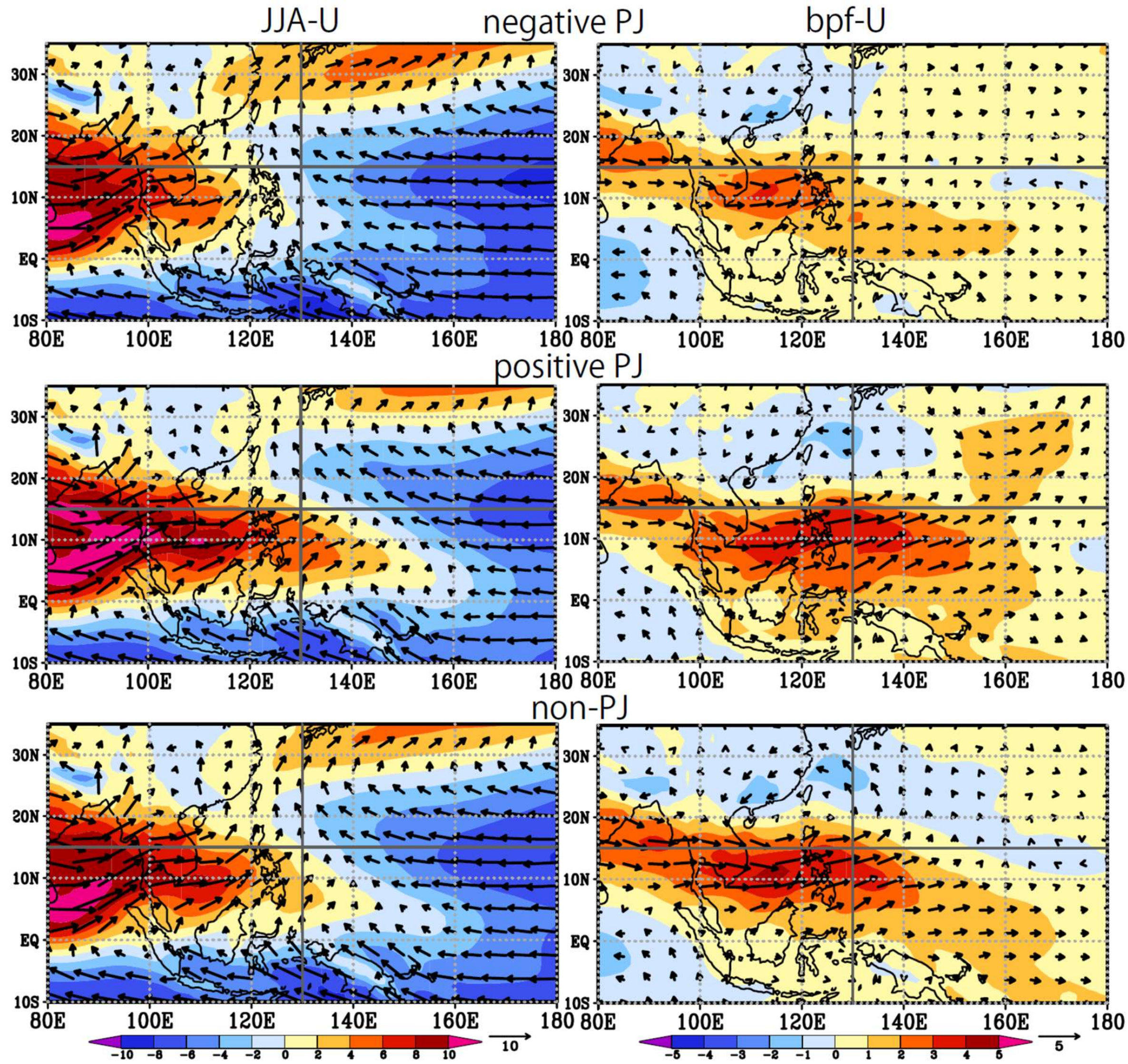

Fig. 13 (left) Seasonal mean zonal winds at 850 hPa averaged for JJA and (right) intraseasonal zonal wind anomalies averaged from BSISO phase 6 to 8 (shading; m s^{-1}). Vectors indicate (left) seasonal mean and (right) intraseasonal wind fields at 850 hPa.

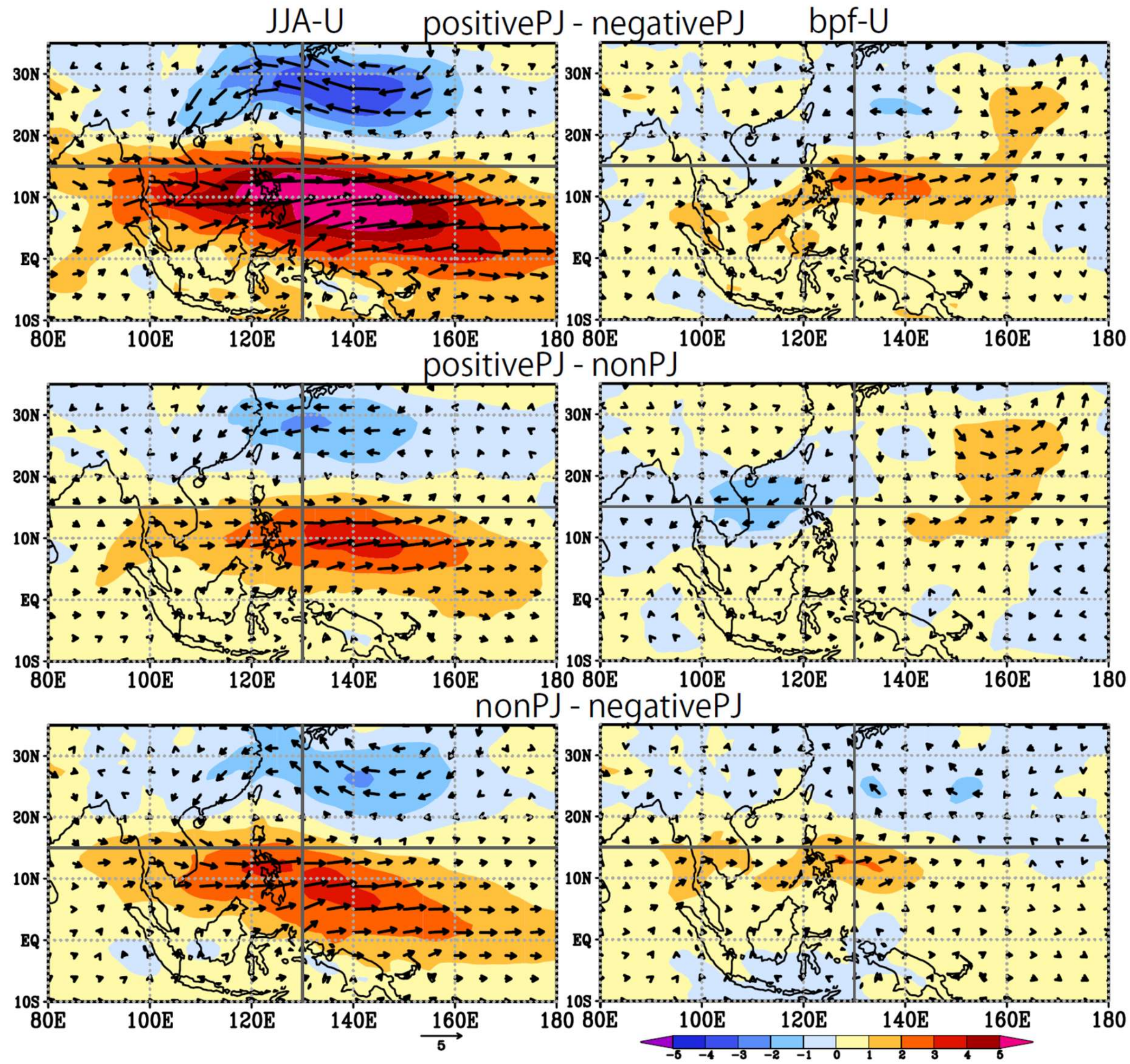

Fig. 14 Differences of (left) seasonal mean zonal winds at 850 hPa averaged for JJA and (right) intraseasonal zonal wind anomalies averaged from BSISO phase 6 to 8 (shading; m s^{-1}) between (upper) the positive and negative PJ years, (middle) positive and non-PJ years, and (lower) non-PJ and negative PJ years. Vectors indicate differences of (left) seasonal mean and (right) intraseasonal wind fields at 850 hPa.